Characterization of Birefringent Distribution of High-Modulus PET Fibers by Senarmont Compensation Method

Weidong Yu

College of Textiles, Donghua University, 1882 West Yan-an Road, Shanghai 200051, China

ABSTRACT: The birefringent distribution of poly(ethylene terephthalate) (PET) fibers has been measured by means of Senarmont's compensation in this article. The difference from the traditional method is that two new approaches (i.e., measuring the shift of either straight fringes on a fiber cylinder or arched fringes on a fiber wedge) are established to figure out the cross-birefringence at different thicknesses of the fiber. Further, the fiber radial birefringent distribution is estimated by both using a series of theoretical models and their algorithms and by measuring with the fiber-wedge method combined with deferential calculation. There exists high coincidence between theoretical and measured values and the PET fiber is a skin-core structure of macromolecular orientation. Meanwhile, the experimental results show that (1) the double-angle measurement set a fiber at both the 0° and the 90° positions is necessary for high accuracy; (2) the setting of each optical element and the fiber is vitally important to obtain the exactly compensated values; and (3) the bulk birefringence is correlated with the measured initial modulus of the PET fibers. © 2003 Wiley Periodicals, Inc. J Appl Polym Sci 91: 598–608, 2004

Key words: birefringence; polyester fiber; Senarmont's method; modulus; polarized microscope

INTRODUCTION

The birefringence of a fiber can be used in the characterization of the macromolecular orientation and tensile properties of the fiber. Therefore, the research of fiber structure and properties have been researched extensively. Many optical methods have been adopted to measure fiber birefringence.[1,2] One of them is the Senarmont compensation method. The polarized microscope used in this compensation consists of a monochromatic light source, a polarizer (*P*), a quart wavelength (λ/4) plate, and an analyzer (*A*). The λ/4 plate and the analyzer make up the compensator of this system. Phase difference δ of a fiber is obtained by rotating *A* for θ angle to produce an extinction line in the central axis of the fiber. The rotating angle (i.e., compensated angle) is equal to half of the phase difference (θ = δ/2),[1] so the birefringence Δ*n* can be calculated as

$$\Delta n = \frac{\lambda}{D}\left(n + \frac{\theta}{\pi}\right) \tag{1}$$

where *D* is the fiber diameter, λ is the wavelength of the monochromatic light, and *n* is the number of interference fringes.

This method has high accuracy and sensitivity because it only measures the fraction part of the phase difference, whereas the integer part can be decided by counting the number of interference fringes on a wedge-shaped fiber. Its traditional application is only to measure the bulk birefringence at the maximum thickness of a fiber.[1,3] This method still seems conventional, although some improvements have been made[4,5] and are unlike other more attractive methods, such as interference microscope,[6–8] IR dichroism,[9] X-ray and electron diffraction, etc.[10–12]

In this author's view, however, the Senarmont method has potential functions in the test of birefringence distribution of fibers. In the present article, two new measuring methods and the corresponding algorithms are defined. The results from the experimental and relevant theoretical models are discussed to illustrate more extensive application of the Senarmont compensation method.

EXPERIMENTAL

Samples and preparation

Samples

High-modulus poly(ethylene terephthalate) (PET) fibers, provided by Azko Ltd., include two series of D10 and C14 PET fibers treated with different conditions, as listed in Table I.

Specimen:	D10 PET fiber					C14 PET fiber				
Method:	Single angle		Double angle		Ratio	Single angle		Double angle		Ratio
No.	Δn_D	CV_S	Δn_D	CV_D	CV_D/CV_S	Δn_D	CV_S	Δn_D	CV_D	CV_D/CV_S
500	0.2046	2.39	0.2045	1.81	0.755	0.1983	4.49	0.1984	2.57	0.573
1500	0.1958	2.91	0.1965	1.83	0.629	0.1917	4.23	0.1898	3.06	0.723
2500	0.1894	2.06	0.1883	1.70	0.825	0.1834	3.71	0.1827	3.23	0.871
3500	0.1861	4.25	0.1858	2.15	0.507	0.1813	4.36	0.1822	2.74	0.630
4500	0.1791	2.85	0.1781	1.80	0.631	0.1787	4.25	0.1805	3.16	0.743
5500	—	—	—	—	—	0.1848	4.71	0.1821	3.24	0.688

Sample preparation

Regarding the Senarmont method, the number of interference fringes in a fiber has to be counted on its cut slope, which should clearly show the interference fringes one by one. Therefore, a smooth-cut plane with a small wedge angle is very key to obtaining the exact number of fringes, particularly for measuring the shift of the fringes in this article. The shakes in cutting must be avoided to decrease the artificial effect,[13] as shown in Figure 2(a).

Measurement

Arrangement of optical components and fibers

The fiber birefringence was measured under 20 ± 2°C and relative humidity (RH) 65 ± 2% by using a polarizing microscope (Olympus BH-2) connected with a CCD camera and a computer. The directions of P, fiber (F), $\lambda/4$ plate, and A in the Senarmont compensation system are relatively important because the rotating direction of A depends on the arrangement of the four elements (P, A, F, and $\lambda/4$ plate). There are four basic forms, as shown in Figure 1. The rotating directions of the analyzer are correct only if the fiber belongs to a positive crystal; otherwise, A should be rotated in reverse for the negative crystals.

Because there exists only the alternation of the rotating direction of A but not the effect on the value of

the compensated angle in different arrangements of the P, A, F, and $\lambda/4$ plate, a more accurate method should be adopted for measuring fiber-compensated angles θ_a and θ_b by setting the fiber on horizontal and vertical positions, respectively, as illustrated in Figure 1(a, b) or (c, d). Therefore, eq. 1 will be transformed into eq. 2. The asymmetry in the optical way[16] can be eliminate by this measurement

$$\Delta n = \frac{\lambda}{D}\left(n + \frac{\theta_a + \theta_b}{2\pi}\right) \qquad (2)$$

Measurement of fiber bulk birefringence

According to the setting, the phase difference δ of a fiber has been obtained by using both single- and double-angle measurement, as shown in Figure 1. The diameter D of the PET fiber is the value averaged from a 10-point measurement along the fiber *in situ*. The fiber bulk birefringence has been calculated by eqs. 1 and 2, respectively.

Measurement of cross birefringence on fiber cylinder

The fiber cylinder method is developed to measure the cross-birefringence in the central part of a fiber by reason of the circular cross section of the fiber. The fiber thickness changes so greatly on two sides of the
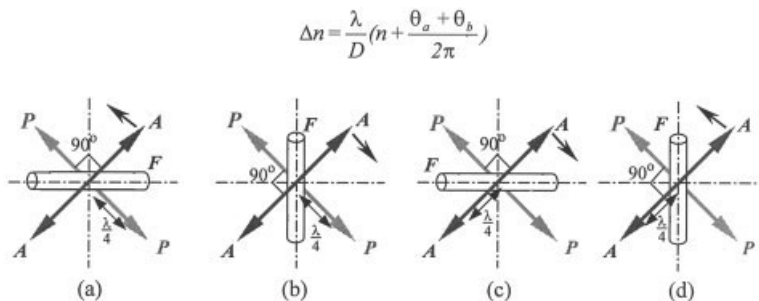

Figure 1 The rotating direction of analyzer (A) and the arrangement of polarizer (P), fiber (F), analyzer (A), and $\lambda/4$ plate ($\lambda/4$) (↔ slow direction).

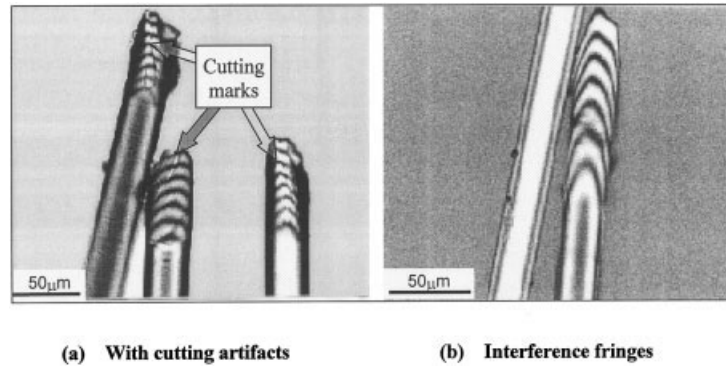(a) With cutting artifacts   (b) Interference fringes

Figure 2 The pattern of fiber interference fringes.

fiber that the shift of interference fringes cannot be seen clearly on the areas, especially for the fibers with high birefringence, as shown in Figure 2. However, the fringes in the central part of the fibers can distinguish at least one pair distinctly [i.e., the shift of the pair of fringes ranging in one or more differences of the optical path can be observed in Fig. 2(b)].

The cross-birefringence in the region has been measured and can also be compared with theoretical models (see Appendix A) to estimate the birefringences in other parts of the fiber. The experimental processing is (1) rotating A to produce the extinction in the central axis of the fiber; (2) rotating A in opposite direction at $\Delta\theta$ as a step (note that $\Delta\theta$ can range from 5° to 20° with the fringes moving to the two edges of the fiber) and measuring the distance X between the two symmetrical strips simultaneously, just as shown in Figure 3(a); (3) finding the thickness T_i and birefringent value Δn_i at each point of X_i, according to the fiber profile (the cross section of the PET fibers is circular); and (4) giving out the birefringent distribution at different thicknesses in cross-direction of the fiber as eqs. 3 and 4:

$$T_i = \sqrt{D^2 - X_i^2} \qquad (3)$$

$$\Delta n_i = \frac{\lambda}{T_i}\left(n + \frac{\theta - \Delta\theta}{180}\right) \qquad (4)$$

Measurement of the cross birefringence on fiber wedge

The measurable range of the shift of fiber interference fringes by the fiber-wedge method is more extensive than that by the fiber cylinder method. The whole range in fiber diameter can be measured actually because of the linear change of thickness in the cut part. The method has been developed not only to measure the cross-birefringence at a certain thickness, as shown in Figure 3(b), but also to estimate the birefringent distribution at fiber radial direction hereinafter.

The measuring steps areas follows.

1. Rotating A at a fixed $\Delta\theta$ (10° or 20° in this present experiment) to make the fringes move from each beginning position to next fringe's position [see Fig. 3(b)] and measuring the distance X_{ij} between zero point and each fringe on every rotation, where i is 0, 1, 2, . . ., n and indicates the interference fringe of $i\lambda$ difference of optical path or $i2\pi$ phase difference, and j is 1, 2, . . ., m and is the rotating times of A.
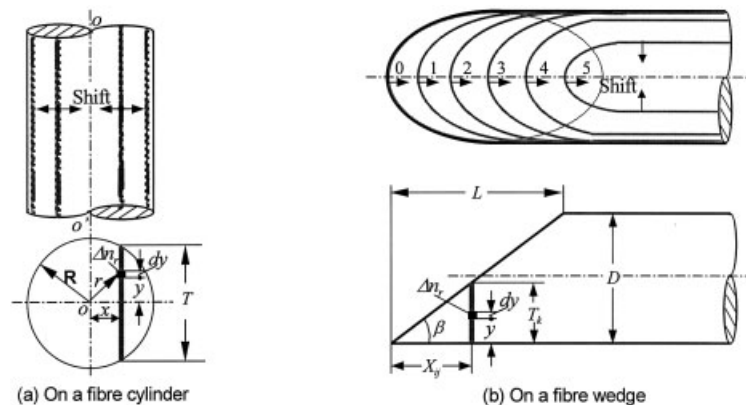

(a) On a fibre cylinder   (b) On a fibre wedge

Figure 3 The schematic calculation of fiber birefringence by the shift of interference fringes.
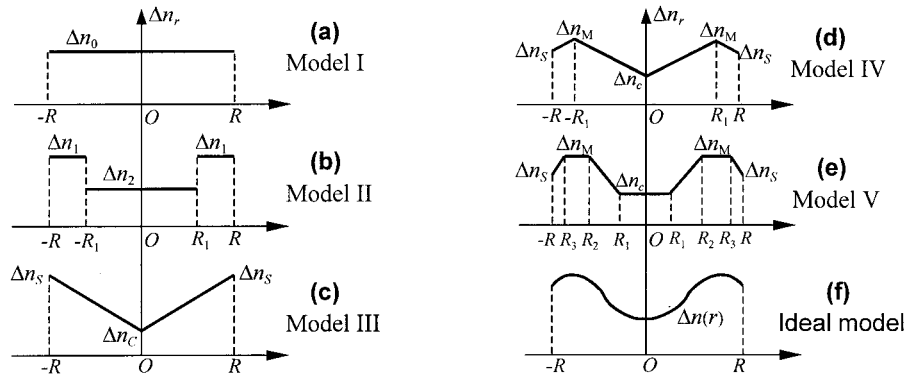
Figure 4 The schematic diagram of the models of different birefringence distributions.

2. Finding the thickness T_k at X_{ij} position and the birefringence Δn_k at the thickness according to eqs. 5 and 6,

$$T_k = X_{ij}\tan\beta = X_{ij}\frac{D}{L} \qquad (5)$$

$$k = \begin{cases} 1,2,\ldots,m,m+1,\ldots,nm-1,nm & \text{(integer part)} \\ nm+1,nm+2,\ldots,nm+m_1 & \text{(fraction part)} \end{cases}$$

3. Giving out the distribution curve of fiber birefringence Δn relative to the thickness T_k.

THEORETICAL MODELS AND ALGORITHMS

Five theoretical models and an ideal (actual) model are shown in Figure 4 and described as follows. The algorithms of the five models are listed in the appendix for the calculation of birefringence on fiber cylinder and wedge, respectively.

Uniform distribution (Model I)

The birefringence along the radial direction is constant for Model I, as illustrated in Figure 4(a)

$$\Delta n_r = \Delta n_0 \quad 0 \le r \le R \qquad (7)$$

The cross birefringence Δn_T at thickness T can be calculated from δ_T as

$$\delta_T = 2\int_0^{T/2}\frac{2\pi}{\lambda}\Delta n_y dy = \frac{2\pi}{\lambda}T\Delta n_T \quad 0 \le T \le D \quad (8)$$

$$\Delta n_T = \frac{\delta_T}{2\pi}\frac{\lambda}{T} = \Delta n_r = \Delta n_0 \quad 0 \le T \le D \qquad (9)$$

$$\Delta n_k = \frac{\lambda}{T_k}\left(i + \frac{j\Delta\theta}{180}\right) \qquad (6)$$

where L is the projecting length of the cutting surface on the fiber axis; and m_1 is the measuring times in frictional part ($m < m_1$).

Skin and core distribution (Model II)

The birefringence in skin layer is different from in core for Model II, as shown in Figure 4(b),

$$\Delta n_r = \begin{cases} \Delta n_1 & R_1 < r \le R \\ \Delta n_2 & 0 \le r \le R_1 \end{cases} \qquad (10)$$

where R_1 is the radius of the interface between the skin and core. The calculations of δ_T and Δn_T from Model II to Model V are listed in eqs. A1–A4 and A5–A8 of the Appendix for the fiber cylinder and the fiber wedge methods, respectively.

Linear distribution (Model III)

The birefringence of Model III increases linearly with the increment of radius [see Fig. 4(c)]

$$\Delta n_r = \Delta n_c + (\Delta n_s + \Delta n_c)\frac{r}{R} \quad 0 \le r \le R \quad (11)$$

where Δn_c and Δn_s are the birefringence at the center and outer layer of a fiber, respectively.

Complex distribution (Model IV and V)

The complex distributions of fiber birefringence, such as Model IV and Model V, are illustrated in Figure 4(d, e), respectively,
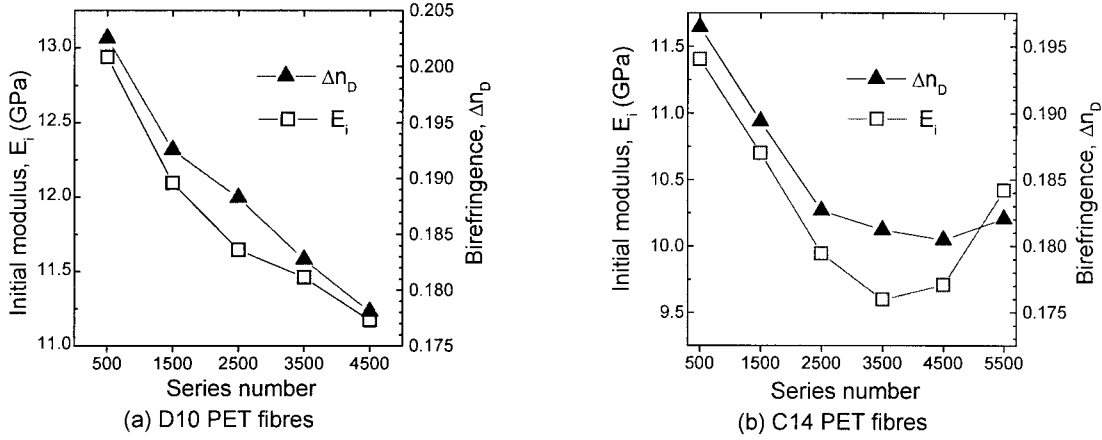
Figure 5 The initial modulus and birefringence of (a) D10 and (b) C14 PET fibers.

Model IV Δn_r

$$= \begin{cases} \Delta n_c + (\Delta n_M + \Delta n_c)\dfrac{r}{R_1} & 0 \le r \le R_1 \\[2ex] \dfrac{r}{R - R_1}(\Delta n_S - \Delta n_M) + \dfrac{R\Delta n_M - R_1\Delta n_S}{R - R_1} & R_1 < r \le R \end{cases}$$

(12)

Model V Δn_r

$$= \begin{cases} \Delta n_c & 0 \le r \le R_1 \\[2ex] \Delta n_c + (\Delta n_M + \Delta n_c)\dfrac{r - R_1}{R_2 - R_1} & R_1 < r \le R_2 \\[2ex] \Delta n_M & R_2 < r \le R_3 \\[2ex] \dfrac{r - R_3}{R - R_3}(\Delta n_S - \Delta n_M) + \dfrac{R\Delta n_M - R_3\Delta n_S}{R - R3} & R_3 < r \le R \end{cases}$$

(13)

where Δn_M is the maximum birefringence of Δn_r, and R_1, R_2, and R_3 are the radiuses at different layers of a fiber.

RESULTS AND DISCUSSION

Bulk birefringence

The bulk birefringence (i.e., the birefringence at the fiber diameter plane) has been measured with the single-angle and double-angle method. It is obvious that the accuracy of the single-angle measurement was lower than that of the double-angle way because of the high coefficient of variation (CV) of the single-angle testing, as listed in Table I. The reason is that the latter can remove the error caused in rotating the analyzer and the asymmetrical effect in the testing. It can also be verified that all the ratios of CV_D/CV_S in Table I are lower than 1 and range from 0.507 to 0.871.

The measured results of PET fiber birefringence and modulus are illustrated in Figure 5. With the increase of serial numbers of D10 fibers, both the birefringence and the initial modulus of the PET fibers decrease significantly; whereas, for the birefringence and modulus of C14 fibers, some are flat and some increase again at a large number, as shown in Figure 5(a, b), respectively. It is indicated from Figure 5(b) that the molecular relaxation of C14 fibers at large numbers has occurred in spinning processing. However, it is obvious from the pair of Δn_D and E_i curves that there should exist high correlation between the fiber birefringence and modulus.

The results obtained by regression analysis are the linear correlation between the two parameters and high-correlation coefficient (i.e., $R = 0.985$ for D10 PET fibers and $R = 0.933$ for C14 PET fibers), as shown in Figure 6(a, b).

Because of the high birefringence of the PET fibers, the difference of average values, Δn_D, between the single- and double-angle method does not seems distinct. However, if the fraction part was only considered, the difference could be significant because the differences of mean and standard deviation are about $10°$ and $10°$-$15°$ of the compensated angle, respectively. Hence, it is necessary to use the double-angle method to achieve a high-accuracy measurement, especially for the fiber with relatively lower birefringence (i.e., fewer interference fringes). This has, in fact, been proven by the higher CV values in Table I and the lower correlation in Figure 6(b) of C14 fibers.

Cross birefringences on fiber cylinder

The fiber cylinder method that investigates the shift of longitudinal fringes at radial direction on a fiber cylinder can give out a group of cross birefringences. Due
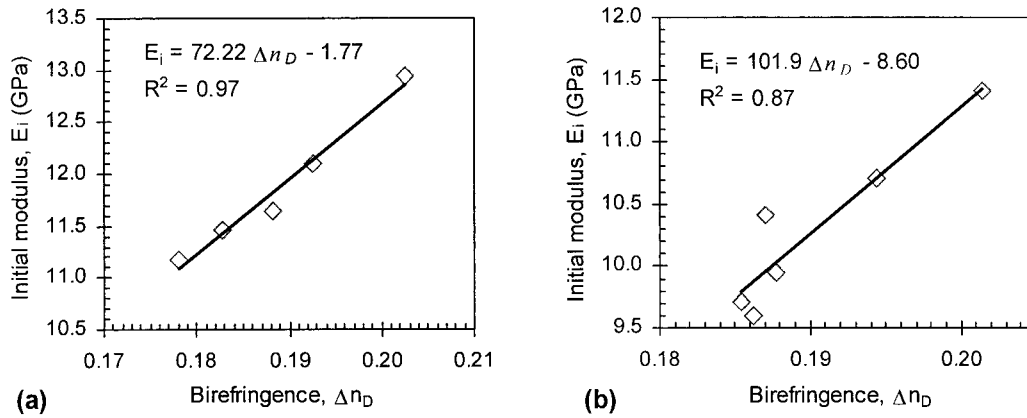
Figure 6 The relationship between the modulus and birefringence of (a) D10 and (b) C14.

to limitation of the side effects of fiber thickness and light refraction on the resolution and the position of interference fringes,[14] respectively, however, it is probable to show the movement of interference fringes in the central part of a fiber (i.e., compensated angles changed from 0° to 180° in the present measurement).

The measured values of D10 3500 fibers in Table II indicate that (1) the cross-birefringence at different thicknesses of the fiber is different; (2) the birefringence in skin layer of the fiber is higher than that in core; and (3) the bulk birefringence Δn_D measured by Senarmont's method is mostly the lowest cross-birefringence Δn_T.

Although the birefringence measured by the fiber cylinder method is one only in near central part of the fiber, as illustrated in Table II, the cross-birefringence in other parts of the fiber can be found by analyzing these data with the theoretical models as mentioned

above. The cross-phase difference δ_T and birefringence Δn_T at T calculated from the theoretical models (i.e., A_κ and B_κ, where κ = I, II, III, IV, and V), and the measured results (A_0, B_0), are shown in Figure 7.

It is obvious that Model I, uniform distribution, disaccords with the experimental results (A_0, B_0). For Model 3, the phase difference has a maximum point, $\delta_{T\max}$, because Δn_T increases rapidly, whereas T decreases slowly with the increment of X in the central part of the fibers. Hence, with the rotation of the analyzer in a positive direction, the extinct phenomenon would occur both at the fiber axis and at the two sides near the central axis of the fiber. The phenomenon, in fact, was not observed of the fiber so that the linear change distribution model may also be eliminated.

It is clear from Figure 7(a) that model II accords much more with the measured results. For a highly accurate prediction, the boundary parameters (Δn_1,

TABLE II
The Results Measured on Fiber Cylinder

θ (°)	X_i (μm)	T_i (μm)	N_δ ($\delta/2\pi$)	Δn_{Ti}
0	0.0	24.5	7.639	0.1840
5	1.7	24.4	7.611	0.1838
10	3.4	24.2	7.583	0.1845
20	5.0	24.0	7.528	0.1852
30	6.3	23.6	7.472	0.1864
40	7.5	23.3	7.417	0.1876
50	8.5	22.9	7.361	0.1890
60	9.5	22.5	7.306	0.1910
70	10.4	22.2	7.250	0.1928
80	11.1	21.8	7.194	0.1944
90	11.8	21.4	7.139	0.1963
100	12.4	21.1	7.083	0.1978
120	13.6	20.3	6.972	0.2020
140	15.0	19.3	6.861	0.2095
160	16.0	18.5	6.750	0.2147
				0.2241
180	17.1	17.5	6.639	
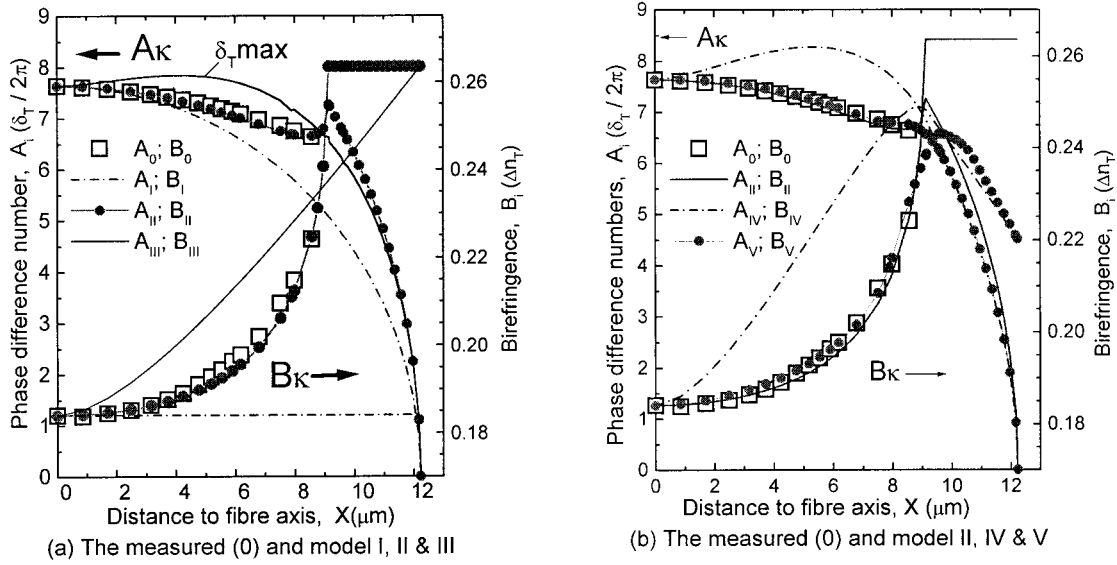
Figure 7 The measured (A_0, B_0) and theoretical (A_κ, B_κ) results on a fiber cylinder.

Δn_2, and D_1) of the model can be evaluated in theory with the measured data. The way is first to evaluate D_1 with eq. 14 and then to find Δn_1 with eq. 15 derived from eqs. A1 and 14, and last, to calculate Δn_2 with eq. 14. Although three measured points may determine the three parameters by eqs. 14–15, a successive approximation calculation to find the optimum boundary parameters has been adopted for all of the measured data to achieve the minimum error between Model II and the measured values

$$\frac{\Delta n_{T_2} - \Delta n_{T_1}}{\sqrt{1 - T_{D_2}^2} - \sqrt{1 - T_{D_1}^2}} = \frac{\Delta n_{T_3} - \Delta n_{T_1}}{\sqrt{1 - T_{D_3}^2} - \sqrt{1 - T_{D_1}^2}};$$

$$T_{D_i}^2 = \frac{D^2 - D_1^2}{T_i^2} \quad (14)$$

$$\Delta n_1 = \frac{\Delta n_{T_1}\tau_2 - \Delta n_{T_2}\tau_1}{\tau_2 - \tau_1}, \quad \tau_i = \sqrt{1 - T_{D_i}^2} \quad (15)$$

$$\Delta n_2 = \frac{D}{D_1}\Delta n_D + \frac{D - D_1}{D_1}\Delta n_1 \quad (16)$$

where Δn_{Ti} is the birefringence measured at the thickness T_i.

It can be found from Figure 7(a) that there still exists some difference between experimental data and theoretical Model II. The main reason may come from the deviation of the theoretical model, besides the noncircular cross section of a fiber, random error, and even eccentric rings. Based on the assumption, further comparisons by means of Model IV and Model V [see Fig. 4(d, e)] have been carried out as indicated in Figure

7(b). Model IV of "- - -" line is unmatched to the measured results "□" in evidence. However, the curve ("—●—") of Model V is much closer to the measured data than that of Model II ("—"solid line). Definitely, Model V is more complex than Model II and has six parameters (i.e., R_1, R_2, R_3, Δn_c, Δn_M, and Δn_S), five of which are independent. These parameters can be decided by means of successive approximation method under the minimum error related to the measured data, as mentioned in Model II.

Birefringent distribution on fiber wedge

The arched fringes on a cut slope of a fiber will shift in the longitudinal direction of the fiber with the rotation of analyzer A. According to the points of the fringes at the fiber axis, as shown in Figure 3(b), and the rotated amount of A, the cross-birefringence at each point can be calculated. The experimental data (B_0) and theoretical-model results (B_κ) are shown in Figure 8. The cross-birefringences at different thickness, T, of the fiber wedge are not the same values, where T represents the distance from fiber surface to cut surface in the diameter plane of the fiber. It is evident that the measurement can avoid the refractive influence because the incident ray is perpendicular to the fiber surface and also to each layer in the fiber.

Obviously, Model I, B_I, is unconformable to the measured results (B_0). Model B_{II} and B_{III} look similar to B_0 to some extent, but Model B_{III} must be eliminated because the fiber is the same one as discussed in the section "Cross birefringences on fiber cylinder." The shape of B_{II} curve accords basically with the measured
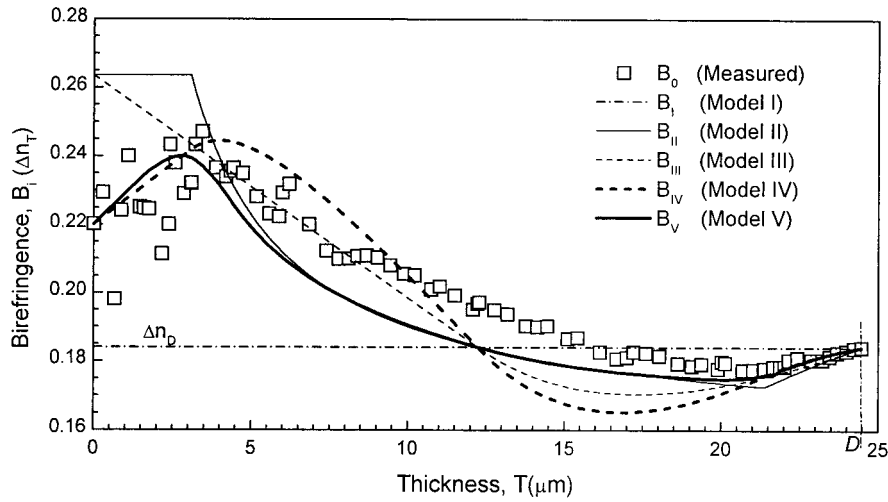
Figure 8 The theoretical and measured curves obtained from the cut slope method.

values, but not at the low thickness, namely the tip of the wedge, as the actual birefringence in the skin layer is not a constant value, as shown in Figure 8.

Model IV shown in Figure 8 is only close to the experimental results at the two sides of the diagram because of the linear function of Δn_r at the skin layer [see Fig. 4(d) $R_1 - R$ and $R_3 - R$]. In the middle part of Figure 8, it is not correct for B_{IV} of Model IV, as the reason has been discussed for Model III as above. Therefore, the most congruous model should locate between Model II and IV and be more approximate to Model II. Accordingly, it is evident that Model V matches the condition for the fiber wedge measure.

For the convenience of calculation and comparison, the same values of six boundary parameters evaluated from the fiber cylinder method have been used to calculate the theoretical cross-birefringence curve (B_V) of Model V. Line B_V of Figure 8 illustrates that Model V accords more with the measured results (B_0 curve) than the other models do, although there are some differences between the measured data and Model V. The main reasons resulting in the difference are probably the nonplanar effect of the fiber wedge and the deviation of the evaluated parameters (i.e., R_1, R_2, R_3, Δn_c, Δn_M, and Δn_S).

One of most significant advantages of the wedge method is that the birefringence at the surface of a fiber can be estimated while $T \to 0$, that is, $\Delta n_S = 0.221$, as shown in Figure 8, although the measured values have high fluctuation. Obviously, it is very difficult to measure and estimate the surface birefringence, Δn_S, accurately by using the fiber cylinder method.

Another of the most important advantages proposed in the present study is that the method observing the shift of the fiber interference fringes on a fiber wedge makes it probable to measure directly the bi-

refringence profile in the radius of a fiber. The principle is described as follows. First, assume that thickness T and phase difference δ at T are known in the wedge method and let $\Delta n_r'$ represent the birefringent value in the dT thick part at radius r of the fiber. Then, s$\Delta n_r'$ can be derived by using

$$\Delta n_r' = \frac{\lambda}{2\pi} \frac{d\delta}{dT} \approx \frac{\lambda}{2\pi} \frac{\delta_{i+1} - \delta_i}{T_{i+1} - T_i} = \frac{\lambda}{\pi} \frac{\Delta\theta}{\Delta T} \quad (17)$$

where $\delta_{i+1} - \delta_i$ is equal to $2\Delta\theta$ because $\delta = 2\theta$ and $T_{i+1} - T_i$ is the thickness difference in one shift caused by rotating the analyzer at $\Delta\theta$. As a result, if $\Delta\theta \to 0$, then

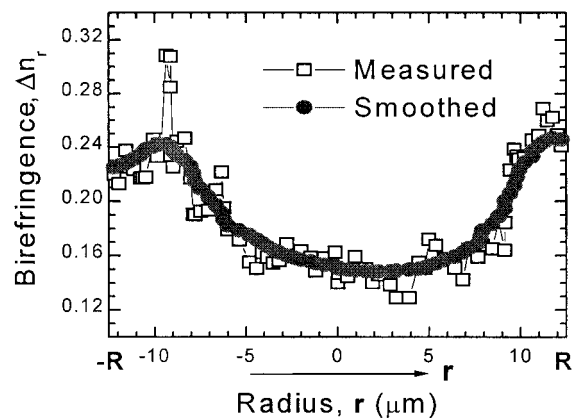$$\Delta n_r' = \frac{\lambda}{\pi} \frac{d\theta}{dT} \quad (18)$$

Figure 9 The real birefringent distribution Δn_r obtained from the fiber wedge method.

Considering the fluctuation of the measured curve of $\Delta n_r'$, the smoothing calculation has been used to make $\Delta n_r'$ curve smooth, as shown in Figure 9. It is obvious that the smoothed curve is approximate to the ideal model, $\Delta n(r)$, in Figure 4(f). Meanwhile, it has also verified the hypothesis of skin-core structure of the PET fibers, the rationality to select Model V, and the coincidence with the results estimated from the fiber cylinder method due to the small side effect. Accordingly, the two important results (i.e., the cross-birefringence at various thickness and the birefringence distribution at radial direction) can be obtained by means of the wedge method.

CONCLUSION

Classical Senarmont's method can be used to measure bulk birefringence of fibers accurately, but can also be developed to be used in the investigation of the cross-birefringence and the radial birefringent distribution of fibers. However, the directions of each optical component and the fiber must be known before the measurement to decide compensated values exactly. At the same time, for obtaining high accurate results and avoiding the asymmetrical effect of a polarimicroscope, the double-angle measurement in which the fiber is set at both 0° and 90° positions should be adopted.

It is verified that there exists high linear correlation between the bulk birefringence and the initial modulus of the high-modulus PET fibers (i.e., correlation coefficient $R > 0.93$) and that the macromolecular orientation structure of the PET fiber is a modified skin-core structure (Model V). It indicates that the fiber modulus can be improved through the modification of molecular orientated arrangement in fiber core and the change of orientation structure can be characterized by the developed Senarmont's method.

Measuring the lateral shift of straight fringes on fiber cylinder can show the birefringent variation at different thicknesses in the central part of a fiber. Combining with the theoretical model analysis, the cross-birefringence in other parts can also be estimated. Measuring the displacement of the arched fringes on fiber cut slope can give out the cross-birefringence at different thicknesses in a whole range of fiber diameter. Moreover, more important is that the fiber wedge method can find out the birefringence distribution in the radial direction of a fiber based on the measured cross-birefringence values or the theoretical models.

APPENDIX

Calculation for the cross birefringence on fiber cylinder

Model II

$$\delta_T = \begin{cases} \frac{2\pi}{\lambda}\left[T\Delta n_2 - \sqrt{T^2 - (D^2 - D_1^2)}(\Delta n_1 - \Delta n_2)\right] & \sqrt{D^2 - D_1^2} \le T \le D \\ \frac{2\pi}{\lambda}T\Delta n_2 & 0 \le T < \sqrt{D^2 - D_1^2} \end{cases} \tag{A1}$$

Model III

$$\delta_T = \int_{T/2}^{T/2} \frac{2\pi}{\lambda}\Delta n_c + (\Delta n_s - \Delta n_c)\frac{\sqrt{x^2 + y^2}}{R}\,dy; \quad x = \frac{X}{2} \quad 0 \le T \le D \tag{A2}$$

Model IV

$$\delta_T = 2\begin{cases} \left[\delta_1 = \frac{2\pi}{\lambda}\int\left[\Delta n_c + (\Delta n_M - \Delta n_c)\frac{\sqrt{x^2 + y^2}}{R}\right]dy\right]_0^{\sqrt{R_1^2 - x^2}} + [\delta_2]_{\sqrt{R_1^2 - x^2}}^{T/2}; & 0 \le x < R_1 \\ \left[\delta_2 = \frac{2\pi}{\lambda}\int\left[\frac{R\Delta n_M - R_1\Delta n_S}{R - R_1} + (\Delta n_S - \Delta n_M)\frac{\sqrt{x^2 + y^2}}{R - R_1}\right]dy\right]_0^{T/2}; & R_1 \le x \le R \end{cases} \tag{A3}$$

Model V

$$\delta_T = 2 \begin{cases} \left[\delta_1 = \frac{2\pi}{\lambda}\int \Delta n_c dy\right]_0^{\sqrt{R_1^2-x^2}} + [\delta_2]_{\sqrt{R_1^2-x^2}}^{\sqrt{R_2^2-x^2}} + [\delta_3]_{\sqrt{R_2^2-x^2}}^{\sqrt{R_3^2-x^2}} + [\delta_4]_{\sqrt{R_3^2-x^2}}^{\sqrt{R^2-x^2}}; \quad 0 \le x < R_1 \\[2em] \left[\delta_2 = \frac{2\pi}{\lambda}\int\left[\Delta n_c + (\Delta n_M - \Delta n_c)\frac{\sqrt{x^2+y^2}}{R}\right]dy\right]_0^{\sqrt{R_2^2-x^2}} + [\delta_3]_{\sqrt{R_2^2-x^2}}^{\sqrt{R_3^2-x^2}} + [\delta_4]_{\sqrt{R_3^2-x^2}}^{\sqrt{R^2-x^2}}; \quad R_1 \le x < R_2 \\[2em] \left[\delta_3 = \frac{2\pi}{\lambda}\int \Delta n_M dy\right]_0^{\sqrt{R_3^2-x^2}} + [\delta_4]_{\sqrt{R_3^2-x^2}}^{\sqrt{R^2-x^2}}; \quad R_1 \le x < R_2 \\[2em] \left[\delta_4 = \frac{2\pi}{\lambda}\int\left[\frac{R\Delta n_M - R_1\Delta n_S}{R - R_3} + (\Delta n_S - \Delta n_M)\frac{\sqrt{x^2+y^2} - R_3}{R - R_3}\right]dy\right]_0^{\sqrt{R^2-x^2}}; \quad R_1 \le x < R_2 \end{cases} \tag{A4}$$

Calculation for the cross birefringence on fiber wedge

Model II

$$\delta_T = \begin{cases} \left[\delta_1 = \frac{2\pi}{\lambda}\int \Delta n_1 dy\right]_0^{T}; \quad 0 \le T \le T_0 \quad (T_0 = R - R_1) \\[1.5em] [\delta_1]_0^{T_0} + \left[\delta_2 = \frac{2\pi}{\lambda}\int \Delta n_2 dy\right]_{T_0}^{T}; \quad T_0 \le T \le T_0 + D_1 \\[1.5em] [\delta_1]_0^{T_0} + [\delta_2]_{T_0}^{T_0+2R_t} + [\delta_1]_{T_0}^{T}; \quad T_0 + D_1 \le T \le D \end{cases} \tag{A5}$$

Model III

$$\delta_T = \begin{cases} \left[\delta_1 = \frac{2\pi}{\lambda}\int\left[\Delta n_c + (\Delta n_S - \Delta n_c)\frac{R - y}{R}\right]dy\right]_0^{T}; \quad 0 \le T \le R \\[1.5em] [\delta_1]_0^{R} + \left[\delta_2 = \frac{2\pi}{\lambda}\int\left[\Delta n_c + (\Delta n_S - \Delta n_c)\frac{y - R}{R}\right]dy\right]_R^{T}; \quad R \le T \le D \end{cases} \tag{A6}$$

Model IV

$$\delta_T = \begin{cases} \left[\delta_1 = \frac{2\pi}{\lambda}\int\left[\frac{R\Delta n_M - R_1\Delta n_S}{R - R_1} + (\Delta n_S - \Delta n_M)\frac{R - y}{R - R_1}\right]dy\right]_0^{T}; \quad 0 \le T \le T_0 \\[1.5em] [\delta_1]_0^{T_0} + \left[\delta_2 = \frac{2\pi}{\lambda}\int\left[\Delta n_c + (\Delta n_M - \Delta n_c)\frac{R - y}{R}\right]dy\right]_{T_0}^{T}; \quad T_0 \le T \le R \\[1.5em] [\delta_1]_0^{T_0} + [\delta_2]_{T_0}^{R} + \left[\delta_3 = \frac{2\pi}{\lambda}\int\left[\Delta n_c + (\Delta n_M - \Delta n_c)\frac{y - R}{R}\right]dy\right]_R^{T}; \quad R \le T \le D - T_0 \\[1.5em] [\delta_{1+2+3}]_0^{D-T_0} + \left[\delta_4 = \frac{2\pi}{\lambda}\int\left[\frac{R\Delta n_M - R_1\Delta n_S}{R - R_1} + (\Delta n_S - \Delta n_M)\frac{y - R}{R - R_1}\right]dy\right]_{D-T_0}^{T}; \quad D - T_0 \le T \le D \end{cases} \tag{A7}$$

Model V

$$\delta_T = \begin{cases} \left[\delta_1 = \frac{2\pi}{\lambda} \int \left[\frac{R\Delta n_M - R_3\Delta n_S}{R - R_3} + (\Delta n_S - \Delta n_M) \frac{R - y}{R - R_3} \right] dy \right]_0^T ; \quad 0 \le T \le R - R_3 \\[2em] \left[\delta_1 \right]_0^{R-R_3} + \left[\delta_2 = \frac{2\pi}{\lambda} \int \Delta n_M dy \right]_{R-R_3}^T ; \quad R - R_3 \le T \le R - R_2 \\[2em] \left[\delta_{1+2} \right]_0^{R-R_2} + \left[\delta_3 = \frac{2\pi}{\lambda} \int \left[\Delta n_c + (\Delta n_M - \Delta n_c) \frac{R - y}{R} \right] dy \right]_{R-R_2}^T ; \quad R - R_2 \le T \le R - R_1 \\[2em] \left[\delta_{1+2+3} \right]_0^{R-R_1} + \left[\delta_4 = \frac{2\pi}{\lambda} \int \Delta n_M dy \right]_{R-R_1}^T ; \quad R - R_1 \le T \le R + R_1 \\[2em] \left[\delta_{1+2+3+4} \right]_0^{R+R_1} + \left[\delta_5 = \frac{2\pi}{\lambda} \int \left[\Delta n_c + (\Delta n_M - \Delta n_c) \frac{y - R_1}{R - R_1} \right] dy \right]_{R+R_1}^T ; \quad R + R_1 \le T \le R + R_2 \\[2em] \left[\delta_{1+2+3+4+5} \right]_0^{R+R_2} + \left[\delta_6 = \frac{2\pi}{\lambda} \int \Delta n_M dy \right]_{R+R_2}^T ; \quad R + R_2 \le T \le R + R_3 \\[2em] \left[\delta_{1+2+3+4+5+6} \right]_0^{R+R_3} + \left[\delta_4 = \frac{2\pi}{\lambda} \int \left[\frac{R\Delta n_M - R_3\Delta n_S}{R - R_3} + (\Delta n_S - \Delta n_M) \frac{y - R_3}{R - R_3} \right] dy \right]_{R+R_3}^T ; \quad R + R_3 \le T \le D \end{cases}$$

(A8)

The definitions of all the symbols in these above equations have been shown in Figure 4. Each birefringence Δn_T can be found by using eq. 9.

References

1. Hartshorne, H. M.; Stuart, A. Crystals and the Polarising Microscope, 4th ed.; Edward Arnold: Sevenoaks, UK, 1970; p 26.
2. Fouda, I. M.; Hamza, A. A.; El-Nicklawy, M. M.; El-Farhaty, K. A. Text Res J 1981, 51, 355.
3. Nahata, A.; Wu, C.; Yardley, J. T. IEEE Transact Instrum Meas 1992, 41, 128.
4. Zimmermann, M.; Schranz, W. Meas Sci Technol 1993, 4, 186.
5. Hariharan, P.; Ciddor, P. E. Meas Sci Technol 1997, 8, 936.
6. El-Tonsy, M. M. J Mater Sci 1991, 26, 2857.
7. Gupta, V. B.; Rama Rao, D. Text Res J 1991, 61, 510.
8. Hamza, A. A.; Sokkar, T. Z. N.; Ramadan, W. A. J Euro Opt Soc, Part A 1992, 1, 321.
9. Wold, E.; Bremer, J.; Handeri, O. J Polym Sci, Part B: Polym Phys 1993, 31, 579.
10. Sotton, M.; Arniaud A. M. Determination of Orientation Parameters in Textile Fibers; Bulletin Scientifique de Institut Textile de France, Aug. 1982; 11, 25–36.
11. Yuan, P.; Sung, C. S. P. Macromolecules 1991, 24, 6095.
12. Davis, H.; Singletary, J.; Srinivasarao, M.; Knoff, W.; Ramasubramanian, M. K. Text Res J 2000, 70, 945.
13. Yu, W. J China Text Univ 1995, 21, 16 (in Chinese).
14. Wu, Z. Z.; Davis, H.; Batra, S. K. Proc R Soc London 1995, 450, 23.